

Three-dimensional imaging technique for direct observation of the complete velocity distribution of state-selected photodissociation products

A. I. Chichinin

Institute of Chemical Kinetics and Combustion, 630090 Novosibirsk, Russia

T. Einfeld, C. Maul,^{a)} and K.-H. Gericke

Institut für Physikalische und Theoretische Chemie, Technische Universität Braunschweig, Hans-Sommer-Strasse 10, 38106 Braunschweig, Germany

(Received 12 September 2001; accepted for publication 27 December 2001)

We report a novel experimental technique provided to study the full three-dimensional velocity distribution of state-selected products of a chemical process. Time-of-flight mass spectroscopy and resonance enhanced multiphoton ionization combined with a novel position sensitive detector (delay-line anode) are employed. The technique has a space resolution of 0.4 mm, a time resolution better than 1 ns, and it provides the possibility to detect several products with a minimal difference between arrival times of 17 ns. One major achievement of the new technique is the possibility to determine the full three-dimensional momentum vectors of a chemical reaction product. This is especially valuable for cases where no symmetry is considered in the process. Second, the high sensitivity of the method allowing to observe single ions enables us to study physical and chemical processes at extremely low densities. Three methods for measuring the temperature of a molecular beam with the technique are demonstrated. A novel result of the present work is the study of angular distribution of NO ions due to electron recoil in the ionization of NO($A^2\Sigma^+$). Finally the advantages of the method are examined by studying the speed distributions of Cl atoms in the photolysis of Cl₂ at 355 nm. © 2002 American Institute of Physics. [DOI: 10.1063/1.1453505]

I. INTRODUCTION

In the last decade there has been considerable interest in the development and application of the photoion imaging technique. Photofragment translational spectroscopy, the resonance enhanced multiphoton ionization (REMPI) time of flight (TOF) technique, the high Rydberg time-of-flight method, and coincidence measurements are the experimental setups that are commonly employed.¹⁻⁵

With the introduction of the photofragment imaging technique a new method was established that allowed one to obtain two-dimensional projections of three-dimensional product distributions with a single measurement.¹ If cylindrical symmetry is conserved the full three-dimensional information may be obtained by a single measurement. At the same time the method allows one to beautifully illustrate the dynamics of a chemical process. Another major step ahead was the development of the velocity map imaging technique that significantly improved the energy resolution of the imaging technique.⁴

Our work was undertaken to develop a novel three-dimensional (3D) photofragment imaging technique for the simultaneous measurement of the velocity (speed and angle) distributions of the products of photodissociation processes. The basic experimental scheme for the imaging technique includes a cold supersonic molecular beam, the state-selective REMPI detection of the photofragments, and a TOF

mass spectrometer combined with a position-sensitive detector (PSD) for ions.

In this context the term “3D imaging” refers to the simultaneous measurement of all three coordinates of a particle which are defined by the spatial position in the two-dimensional plane defined by the surface of the PSD and by the time of arrival at the detector (the third dimension) of the ionized product of a photodissociation process. The transverse velocity components (v_x, v_y) of the initial velocity of the product are determined from the measured two-dimensional impact position on the PSD surface, while the measured time of arrival gives the longitudinal component (v_z) of the velocity. Hereafter the laboratory axis X , Y , and Z are directed along the laser beam, the molecular beam, and the accelerating electric field, respectively. Direct determining the 3D velocity distribution of the product provides complete information about the photodissociation process.

What are the principal advantages of the 3D imaging technique over the two-dimensional (2D) “velocity map imaging” method? To analyze 2D “velocity map” images the Abel inversion algorithm or the forward convolution analysis are usually used.^{3,6} The Abel algorithm is rather simple, but it has several limitations: first, it assumes cylindrical symmetry of the initial 3D distribution, second, the electric field vector E of the dissociative radiation must be perpendicular to the Z axis ($E \perp Z$), and third, a rather large number of data points is necessary to reconstruct the 3D distribution of the ions. The forward convolution analysis is more powerful, but it is computationally expensive and, in general, does not lead to unique solutions.

^{a)}Electronic mail: c.maul@tu-bs.de

In contrast to the 2D method, the 3D imaging approach is quite straightforward. Integration techniques, such as the Abel inversion algorithm or the forward convolution analysis, are not required. Moreover, the 3D imaging approach is more universal: it can be used with any polarization geometry, including the common cases ($E\parallel Z$) and ($E\perp Z$), and it does not assume any symmetry of the initial 3D distribution. There are several reasons that may break the cylindrical symmetry of the initial fragment distributions. First, it is the alignment of the parent molecules in the cold molecular beam: collisions occurring during the supersonic expansion can produce the molecules in their lowest rovibrational states with alignment of the rotational angular momentum perpendicular to the axis of the molecular beam.^{7,8} The alignment degree can be rather large, strongly varies with the molecular speed, and it is expected to depend on the used experimental conditions.⁸ The phenomenon was observed for O_2 (Refs. 9 and 10) and N_2 (Ref. 11) seeded in lighter carriers, for CO (Ref. 12) seeded in He, and for N_2^+ drifted in He.¹³ Recent evidences have also been provided for benzene.¹⁴ This effect changes the relative intensities of ions traveling along the X and the Y axis. Second, it is the alignment of the products that may happen due to a correlation between the J and v vectors,^{3,15–17} where J is the rotational angular momentum and v is the recoil velocity of the products. The 3D imaging approach does not remove this effect, but it provides much more possibilities to study it. Third, the length of the spot of the REMPI laser (usually about 0.5 mm) is small, but not negligible in comparison with the size of the ion distribution over the PSD surface (in the range of a few centimeters). It makes the speed distribution along the Y axis wider than that along the X axis.

The 3D imaging technique is the most appropriate method for studying the photofragment angular momentum alignment as a function of recoil angle (v – J correlation) in photodissociation processes, since the angular distributions of the photofragments are measured directly. Otherwise the 3D distributions must be reconstructed from the 2D images, as it was done, for example, in the studies of photodissociation of Cl_2 .^{16,17}

Another principal advantage of the 3D imaging technique is the possibility to perform coincidence measurements: that is, to simultaneously detect two fragments generated in the same elementary process from the same parent molecule.^{18–21} Coincidence measurements are especially important for the study of the dynamics of photoinduced three body dissociations ($ABC+h\nu\rightarrow A+B+C$) since they simultaneously provide 3D velocities of two fragments while the 3D velocity of the third fragment can be calculated from the conservation law for linear momentum.^{5,22}

II. EXPERIMENT

The experimental apparatus used here is similar to that described elsewhere^{23–25} except that a continuous molecular beam and a new PSD are used. The experimental apparatus is depicted schematically in Fig. 1. It consists of a TOF mass spectrometer (MS), a molecular beam, a PSD, and an optic system based on a Nd:YAG laser-pumped dye laser.

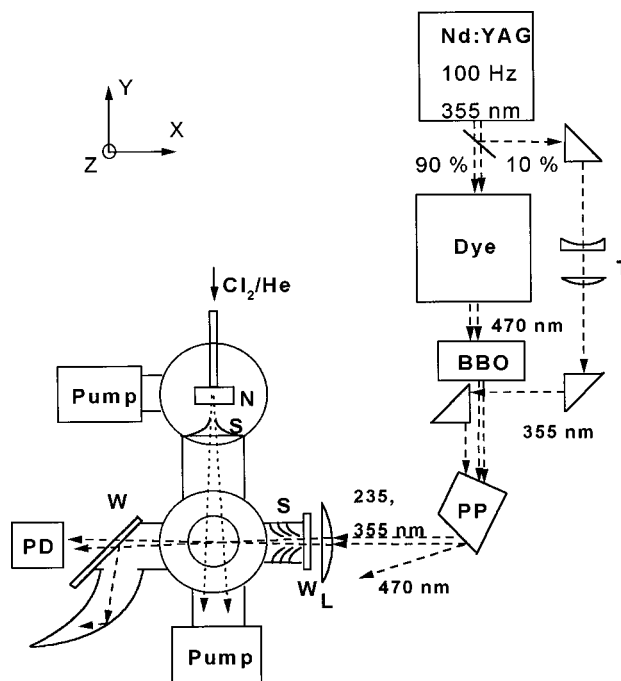


FIG. 1. The 3D imaging experimental setup. PP: Pellin–Broca prism, W: quartz window, L: lens, PD: photodiode, Pump: turbomolecular pump, T: telescope system, N: nozzle, and S: skimmers for light and molecular beams. Molecular and light beams are shown by dotted and dashed lines, respectively. The DLD is located perpendicular to the laser beam and the molecular beam above the paper plane. Also shown is the axis system used throughout this work.

A. Laser and optics systems

The optic system generally comprises two pulsed lasers. The first one is a photolysis laser for the photodissociation of the parent molecule, the second one is a probe (ionizing) laser for the state-selective detection of the neutral photofragment by the REMPI technique. If the wavelength of the second laser is suitable for photolysis, then a single-laser configuration is possible.

State-selective detection of Cl atoms in the $^2P_{3/2}$ ground state was achieved by (2+1) REMPI via the $4p^2D^0_{3/2} \leftarrow 3p^2P_{3/2}$ transition at 235.336 nm.²⁶ NO($v=0$) molecules in different rotational states are detected by (1+1) REMPI via the $A^2\Sigma^+ \leftarrow X^2\Pi$ around 226.2 nm.²⁷ For this purpose, a Nd:YAG laser-pumped dye laser (Coherent Infinity/Lambda Physik Scanmate) operated with Coumarin-47 dye and frequency doubling in a BBO crystal was used. The radiation with doubled frequency was separated by a Pellin–Broca prism. For detection of NO only the probe laser was used. In experiments with photolysis of Cl_2 the third harmonic of the Nd:YAG laser (355 nm) was used to dissociate Cl_2 molecules. In this case, the Pellin–Broca prism was used to combine the two laser beams to a single one with two wavelengths (355 and 235.336 nm). The laser radiation was focused by a lens ($f=18$ cm) into the ionization chamber of the TOFMS. A photodiode was used after the ionization chamber to monitor the power of each laser shot.

Note that the adjustment of the optic system and the ion detection system may be rather laborious; hence we recommend using a molecular beam with a NO gas mixture for these preliminary works because the NO molecules in differ-

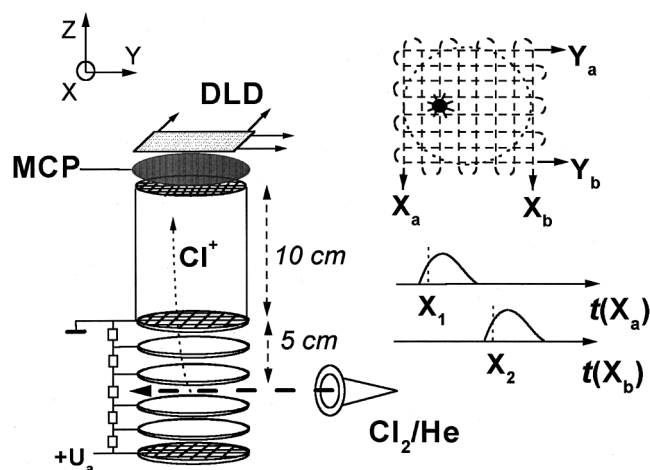


FIG. 2. Left: Schematic diagram of the TOFMS. A homogenous electrostatic field in the acceleration region is created by the ring electrode system. The system is limited by metallic meshes from both sides. After the drift region the ions impinge on the MCP. Electrons from the MCP are accelerated towards the DLD. Right: Illustration of the DLD principle. The ion impinging on the MCP induces two pulses on each delay line traveling to the respective ends X_a , X_b , Y_a , and Y_b of the lines. The time differences $X_2 - X_1$ and $Y_2 - Y_1$ define X and Y positions on the DLD.

ent rotational states may easily be detected by a single-laser setup with a high sensitivity using a (1 + 1) REMPI scheme.

B. Time-of-flight mass spectrometer (TOFMS)

The vacuum system of our home-built single-field TOFMS consists of jet and ionization chambers separated by a skimmer (diameter of 0.4 mm) evacuated to a base pressure of 10^{-7} mbar by two turbomolecular pumps. A cold continuous molecular beam is obtained by a supersonic expansion of a gas mixture at a pressure of 1.5–6 bar through the 20 μm nozzle. The distances nozzle–skimmer and skimmer–laser beam are 1.5 and 30 cm, respectively. Hence the diameter of the molecular beam in the center of the ionization chamber is 8 mm.

Cl^+ or NO^+ ions are generated by REMPI in the acceleration region of the ionization chamber of the TOFMS. The TOFMS includes an acceleration region of 5 cm length and a drift region of 10 cm length. Ions are detected by a double stage multichannel plate (MCP) assembly (Roentdek, diameter of 8 cm). The MCP signals were monitored by a digital oscilloscope (LeCroy 9450).

In the ionization chamber the skimmed molecular beam is intersected by the probe and the photolysis laser beams whose propagation direction (X axis) is perpendicular to the molecular beam propagation axis (Y axis). The ionization chamber is shown in Fig. 2. Products generated in the photodissociation are state-selectively ionized by the probe laser and are accelerated along the Z axis towards the field-free drift region of the TOFMS. Typically, electric field strengths of 3000 V/m are realized by applying an acceleration voltage of $U_a \approx 300$ V to the acceleration stage.

C. Delay line detector

In this section we describe the special case of a PSD, which is called a delay-line detector (DLD). The DLD con-

sists of a delay-line anode introduced into the ionization chamber right behind the MCP assembly. An additional potential (≈ 300 V) applied between the MCP and the DLD accelerates the electrons to the delay-line anodes. Note that the MCP signal itself, produced by incoming ions and picked up from the charging circuit of the MCP assembly, is only used for adjustment purposes and for the measurement of the mean time-of-flight averaged over all observed single ion events, whereas all quantitative information on the three-dimensional velocity components of each individual ion is obtained from the DLD signal.

The idea of a DLD consists of what follows: a signal induced somewhere on a delay line (basically nothing more than a long wire) propagates in both directions towards the ends of the line where impedance adjusted circuits pick it up for further processing. By measuring the time period between the signal arrival times on both ends of the delay line one can determine a position of the signal source on the delay line.

The technical realization of the DLD itself is described in detail in the literature.^{28–30} Briefly, it consists of two individual delay lines oriented orthogonal to each other, thus forming the XY plane. A metal body supports ceramic rods placed on the edges, and the delay lines are wound helically on this 8×8 cm supporting plate. By this folding technique, a propagation delay of 20 ns/cm and a total single-pass delay of 150 ns is realized, corresponding to a physical length of the delay line of 45 m. Each delay line consists of a pair of wires wound parallel to each other, with a small potential difference (30 V) applied between the two wires of each pair. Thus the incoming charge cloud from the MCP induces a differential signal on each delay line pair that propagates to the delay line ends where it is picked up by a differential amplifier.

D. DLD data analysis

A block diagram of the electronic read-out circuit for the DLD is shown in Fig. 3. The output charge from the MCP resulting from every single incoming ion or photon (“event”) produces altogether four differential signals, two on each delay line pair; the pairs are denoted X_a , X_b , Y_a , and Y_b . These signals are decoupled from the dc voltages on the wires, amplified, and transmitted to constant fraction discriminators, then to demultiplexers, and then to time-to-digital converters. The time-to-digital converters are gated to capture only the mass of interest.

Finally, one event produces two pairs of times, (X_1, X_2) and (Y_1, Y_2) , on the delay lines that are wound along the X axis and the Y axis, respectively. The X and Y coordinates of a single event in time units may be calculated as $(X_1 - X_2, Y_1 - Y_2)$; and the time of the event (corresponding to the Z coordinate) usually is calculated as $(X_1 + X_2 + Y_1 + Y_2)/4$. Thus the DLD yields the 3D coordinates of each single event. The latter condition allows one to distinguish between true and false events: the event time provided by the different delay lines must coincide, hence $X_1 + X_2 = Y_1 + Y_2$. Only those events that obey this condition are taken into account, and all others are ignored. If more than one ion

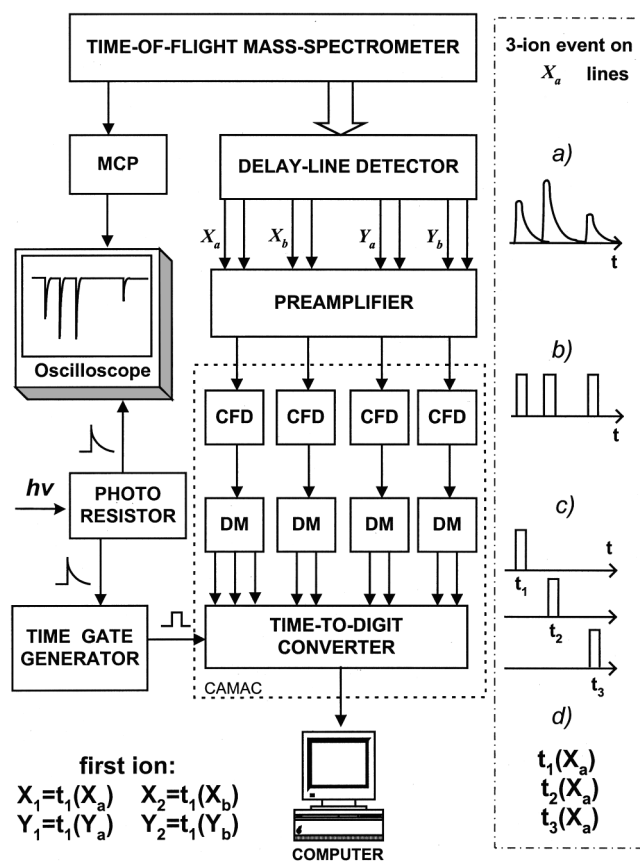


FIG. 3. Block diagram of the electronic read-out circuit for the DLD. CFD: constant fraction discriminator, DM: demultiplexer. The X_a , X_b , Y_a , and Y_b outputs of the DLD give X_1 , X_2 , Y_1 , and Y_2 time moments for each ion. In dashed frame: Example of the temporal signal profile of a three ion event on the X_a line (a) initially, (b) after the CFD, (c) after the DM, and (d) finally, as $t_1(X_a)$, $t_2(X_a)$, and $t_3(X_a)$ which are the X_1 time moments of the first, second, and third ion, respectively.

per laser pulse strikes the MCP assembly, then each delay line produces a series of pulses and the criterion $X_1 + X_2 = Y_1 + Y_2$ allows one to correctly assign individual pulses to individual ions.

The present DLD electronics are able to detect no more than two ions, since two-event demultiplexers are used. But on one of the lines (X_a) there is a three-event demultiplexer. It is used to check if the number of pulses (ions) is larger than two. This information is important for coincidence measurements in which the simultaneous detection of two photofragments from the same parent molecule is necessary.

Since our DLD is not able to detect more than two ions in one shot, we usually decrease the energy of the probe laser in order to detect only one ion in several shots; this helps to avoid space-charge problems and guarantees obtaining the correct distribution over time-of-flight. The repetition rate for the probe laser shots is limited by the Nd:YAG laser (≤ 100 Hz).

E. Time and space resolution of spectrometer

The space resolution of the REMPI/TOF/DLD spectrometer was determined in experiments with a fine metallic mesh (0.2 mm in diameter) placed just in front of the MCP assembly which was irradiated by α particles. The wires of the

mesh appeared as a geometric projection on the DLD, and the dimensions of the projection allowed us to determine the spatial resolution of the detector. From the analysis of the image we have obtained a space resolution of the DLD to be 0.37 mm, this is the width of the DLD image of an infinitely thin wire.

Assuming that the time resolution is determined by the constant fraction discriminators, which may be treated as independent sources of noise, and using the space resolution, we can estimate the time resolution of the DLD to be 0.25 ns. This number is typical for delay-line detectors. But the time resolution of the whole REMPI/TOF/DLD spectrometer is usually limited by the duration of the probe laser pulse which is of the order of 3–5 ns if a Nd:YAG pump laser is used.

The DLD provides the possibility to detect several products per laser shot, provided a minimal difference between arrival times of 17 ns is maintained.

F. Why DLD?

Note that the common PSD for an ion imaging experiment is a phosphor screen as optically collecting anode combined with read-out by video camera and/or charge-coupled device (CCD) camera.^{3–5,31} However, this “classical” method is optimized for the 2D imaging of single particles, obtaining the time-of-flight information is rather difficult because of rather low time resolution of the phosphor screen (40–100 ns).

The space resolution of the phosphor screen is slightly better than that of the DLD: the image of one ion on the phosphor screen has the size of ≈ 0.25 mm,³² which is 1.5 times smaller than space resolution of our DLD. However, our DLD is larger than a typical phosphor screen, hence the resolution of our picture is not less than that obtained with the phosphor screen. Also, the construction of our PSD is simpler and less expensive than a CCD camera.

III. CHARACTERIZATION OF MOLECULAR BEAMS

A. How to measure the temperature of the molecular beam

The knowledge of the temperature of the molecular beam is often useful: for example, the temperature may have an effect on the speed distribution of the photodissociation products (see the next section). Our technique provides an excellent possibility to study molecular beam properties because it provides the quantum state specific 3D momentum vector. In this article we discuss three methods to measure the temperature of the molecular beam.

Figure 4 shows examples of the space distribution of NO^+ ions at different acceleration voltages that are equivalent to different times-of-flight. In these experiments, a diluted (10^{-4}) mixture of NO in B (B=Ar, He, or N_2) was expanded through the nozzle and NO was detected by (1 + 1) REMPI at 226.2 nm. The analysis of the space distributions of NO along the Y axis has shown that the distribution has a Gaussian profile:

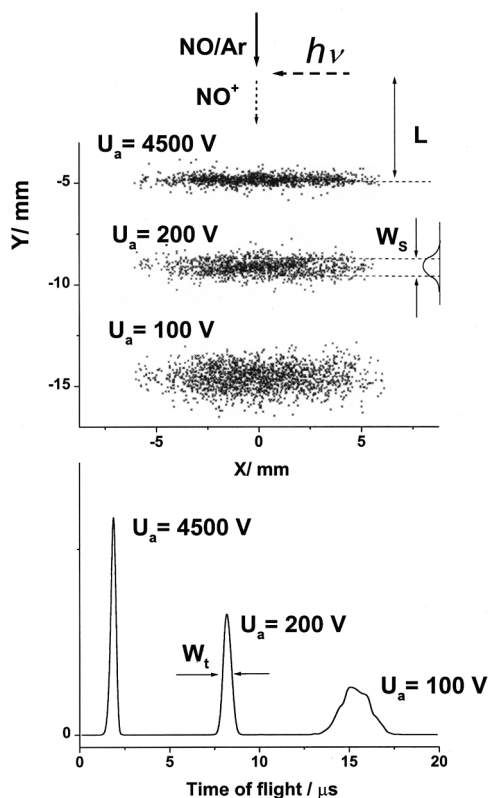


FIG. 4. Upper panel: Space distribution of NO^+ ions from the 226.2 nm ionization of NO for different acceleration fields. Lower panel: Distribution of the time-of-flight for the same three groups of ions. For illustrative purposes the widths W_t of the TOF profiles $t_1(X_a)$ are increased by a factor of 100.

$$W(y) \sim \exp\left[-\ln 2 \left(\frac{2(y-L)}{W_s}\right)^2\right],$$

where y is the space coordinate along the molecular beam axis, L is the position of the molecular beam, and W_s is the full width at half maximum (FWHM) of the space distribution. The variations of W_s and L with time-of-flight t_0 are shown in Figs. 5 and 6, respectively, and can be used to

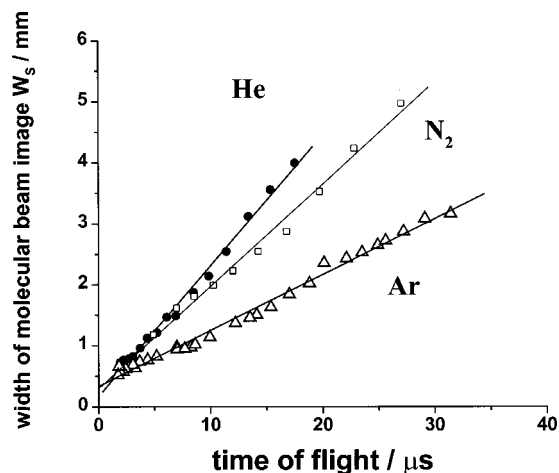


FIG. 5. Plot of the width of the space distribution W_s (Fig. 4) vs time-of-flight for NO/B (B=He, Ar, or N_2). The data exhibit the expected linear dependences the slopes of which give the temperatures of the NO/B molecular beams, see Eq. (2).

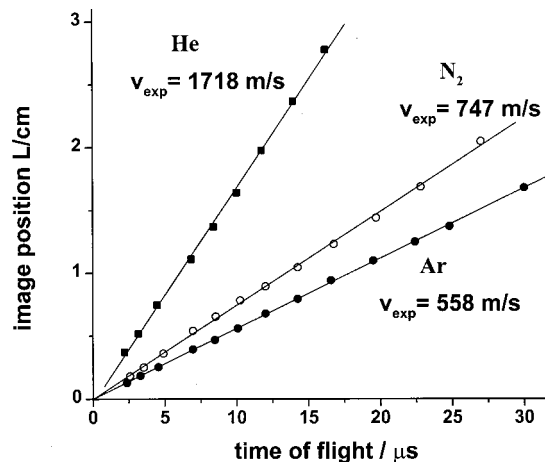


FIG. 6. The plot of the position L (Fig. 4) vs time-of-flight for NO/B (B=He, Ar, or N_2) yields straight lines the slopes of which are the speeds of the NO/B molecular beams.

calculate the translational temperature T_Y and the speeds v_{exp} of the molecular beam.

Figure 5 is an experimental plot of the width W_s as a function of the time-of-flight t_0 . The Gaussian profile of the space distribution $W(v_y)$ comes from the one-dimensional Gaussian speed distribution over the Y axis which is characterized by the temperature T_Y

$$W(v_y) = W_y \exp\left[-\frac{M_{\text{NO}}(v_y - v_{\text{exp}})^2}{2kT_Y}\right], \quad (1)$$

where M_{NO} is the mass of the NO molecule.

Substituting here $v_y - v_{\text{exp}} = (y-L)/t_0$ one can find the relation between W_s and T_Y :

$$T_Y = \frac{M_{\text{NO}}(dW_s/dt)^2}{8k \ln 2}, \quad (2)$$

where dW_s/dt is the slope of the linear fit to the data in Fig. 5. The experimental results on T_Y are summarized in Table I.

In the second method the internal temperature of the beam T_{calc} may be obtained from the difference between experimental speed of the beam v_{exp} and the maximum theoretical speed of the beam v_{max} . The method to obtain the speeds v_{exp} of NO/B (B=He, Ar, or N_2) molecular beams is quite straightforward: the speeds are the slopes of the linear fits to the data in Fig. 6, $v_{\text{exp}} = dL/dt$. The maximum theoretical speed of the molecular beam v_{max} may be calculated as^{33,34}

$$v_{\text{max}} = \sqrt{\frac{\gamma}{\gamma-1}} \sqrt{\frac{2kT_0}{M_B}}, \quad (3)$$

where M_B is the mass of the buffer gas molecule, k is the Boltzmann constant, $T_0 = 295$ K is the room temperature, and $\gamma = C_p/C_v$. The γ parameter is equal to 5/3 and 7/5 for an atomic and a diatomic buffer gas, respectively. Equation (3) assumes that all rotational and translational energies of the molecule are transformed to kinetic energy of the beam: the colder the beam, the closer are v_{max} and v_{exp} values. The internal temperature of the beam T_{calc} may be obtained from the difference between these speeds:

TABLE I. Summary of temperatures of the molecular beams for different buffer gases.

Gas	v_{\max}^a m/s	v_{\exp}^b m/s	T_Y^c K	T_{rot}^d	T_{calc}^e K
Ar	554	558 ± 4	3.5 ± 0.5	3.0 ± 0.5	-4 ± 5
He	1751	1718 ± 12	12.3 ± 2	8 ± 2	11 ± 5
N ₂	783	747 ± 12	12.7 ± 2	12 ± 2	26 ± 9
H ₂	2931	2041 ± 40			152 ± 6

^a v_{\max} is the maximum beam velocity which has been calculated assuming complete cooling to a temperature of 0 K, calculated with Eq. (3).

^b v_{\exp} is the experimentally observed value.

^c T_Y is the translational temperature of the molecular beam derived from the spread in the v_y velocity component (in beam direction), extracted from the broadening of the impact position on the DLD, see Eq. (2).

^d T_{rot} is the rotational temperature of the NO molecule extracted from spectroscopic measurements of the intensities of rotational transitions.

^e T_{calc} is the internal temperature of the beam calculated from the difference between v_{\exp} and v_{\max} , see Eq. (4).

$$T_{\text{calc}} = T_0 [1 - (v_{\exp}/v_{\max})^2]. \quad (4)$$

The values for v_{\exp} , v_{\max} , and T_{calc} are listed in Table I.

The rotational temperature T_{rot} of NO may be obtained from experimental rotational spectra, this is the third method for determination of the internal temperature of the molecular beam. Our technique provides some advantage over conventional REMPI spectroscopy. One problem of the spectroscopy in the cold molecular beam is the contribution of room-temperature background molecules and impurities which make the spectra more difficult to analyze. In time-of-flight experiments with a perpendicular geometry of molecular beam and spectrometer axis it is easy to distinguish between contributions from the molecular beam and background contributions since the particles which belong to the molecular beam are situated on a very small area of the DLD which is shifted from the axis of the laser by the distance $v_{\exp}t_0$. Examples of REMPI spectra of NO in the Ar and He molecular beams are shown in Fig. 7. Least-squares fit of such experimental spectra to the theoretical spectra was used to deter-

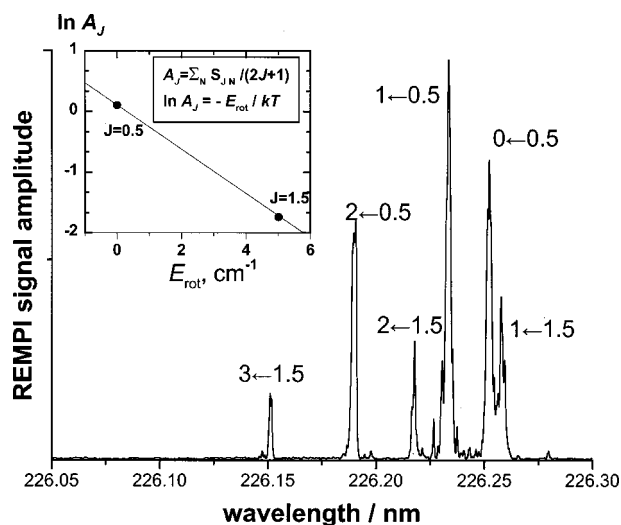


FIG. 7. Rotational REMPI spectrum of NO in a cold Ar molecular beam. Only ions from the molecular beam are taken into account. The $N \leftarrow J$ assignment of the strongest rotational transitions is indicated. In the left corner: Simplified determination of the rotational temperature T_{rot} of NO. S_{JN} is the peak area for a single $N \leftarrow J$ transition, and A_J is the cumulated peak area for all transitions originating from a single J level after correcting for degeneracy.

mine the rotational temperature T_{rot} of NO in Ar, He, and N₂ molecular beams. In this analysis the strengths for rotational transitions were taken from Ref. 35.

Note that all three temperatures, T_{rot} , T_{\exp} , and T_Y , have different nature and in principle they may be different. The largest must be T_{rot} , particularly for the molecules with large rotational constants; the smallest must be T_Y . Nevertheless, in our case there exists a satisfactory consistency in all three temperatures as summarized in Table I.

B. Ionization of NO

The speed distribution along the Z (time) axis is not Gaussian, it depends strongly on polarization of the laser radiation. Time-of-flight profiles of NO detected by $(1+1)$ REMPI via $[A^1\Sigma^+ \leftarrow [A^2\Sigma^+, N=1] \leftarrow [X^2\Pi_{1/2}, J=0.5]]$ transitions at 226.229 nm at different polarizations of the laser radiation are shown in Fig. 8. Also shown are time windows $[t_0 - \Delta t, t_0 + \Delta t]$, where Δt is determined by the electron recoil in the ionization of NO, it may be calculated from the geometry of the TOFMS and the speed of the NO^+ ion due to the electron recoil. The speed may be calculated as

$$v_{\text{NO}} = (m_e/M_{\text{NO}}) \sqrt{2(2h\nu - I_{\text{NO}})/m_e} = 14.1 \text{ m/s}. \quad (5)$$

Here m_e is the mass of electron, $h\nu$ is the photon energy ($\lambda = 226 \text{ nm}$), and $I_{\text{NO}} = 9.2639 \text{ eV}$ is the first ionization potential of NO.

One can see in Fig. 8 that the TOF profiles have no sharp corners and they spread outside this time range. Hence there are other broadening mechanisms, apart from the ionization process. One of them, surely, is the duration of laser pulse ($\sim 5 \text{ ns}$). Another may be the interaction between NO^+ and other ions. From the analysis of the time-of-flight spectra we can determine, for example, the β parameter for the ionization of $\text{NO}(A^2\Sigma^+)$ in different rotational states. Further work is in progress to measure and analyze the TOF profiles accurately.

IV. 3D VELOCITY DISTRIBUTION OF PHOTOFRAGMENTS

A. Model system: Photolysis of Cl₂

The quality of the developed technique was examined by studying the well-known decay of molecular chlorine, Cl₂

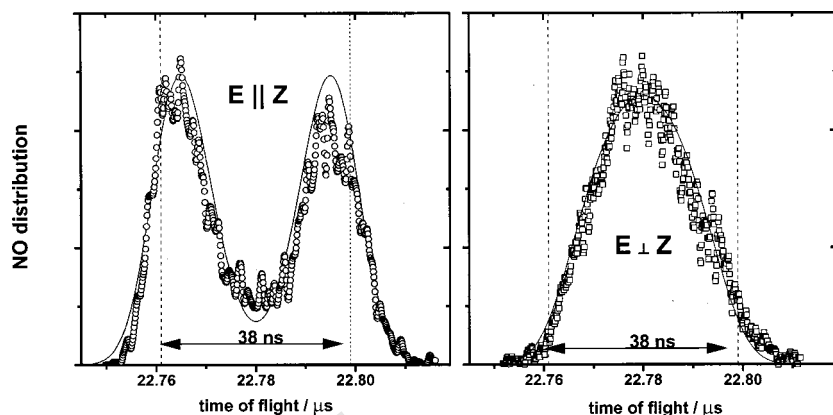


FIG. 8. Time-of-flight profiles of NO^+ ions obtained from ionization of $\text{NO}(A^2\Sigma^+, N=1)$ for different polarization geometries at 226 nm. The time range $t_0 \pm \Delta t$ is shown by two dashed lines. The solid lines result from a least-squares fit of the theoretical expressions accounting for profile broadening from a spatially anisotropic ion distribution to the experimental points. The fit yields an anisotropy parameter $\beta = 2.0 \pm 0.2$.

$+h\nu$ (355 nm) $\rightarrow 2\text{Cl}(3p^2P_{3/2})$. In the experiments the third harmonic of a Nd:YAG laser (355 nm) was used to photolyze Cl_2 , and a Nd:YAG laser-pumped dye laser was used for the (2+1) REMPI detection of ground state $\text{Cl}(^2P_{3/2})$ atoms at 235.336 nm. The yield of spin-orbitally excited $\text{Cl}(^2P_{1/2})$ for the photolysis is known to be negligible.^{36,37} In our measurements the wavelength of the probe laser radiation was scanned over the Doppler broadened absorption line in order to realize an unbiased detection of all Cl atoms regardless of the v_x component of their velocity.

An example of 3D speed distributions of Cl atoms obtained in this way is shown in Fig. 9 (left). The 3D image on this figure consists of two overlapping spherical distributions: the first one corresponds to fragments from background Cl_2 at room temperature, and the second one corresponds to fragments from cold Cl_2 in the molecular beam. Least-squares fit of the experimental data gives the centers of these distributions. Thus from Fig. 9 one may easily determine the speed of the molecular beam as $v_{\text{exp}} = \Delta L/t_0$, where ΔL is the distance between the two spheres. The speed of the Cl_2/H_2 molecular beam was determined by this method only (see Table I).

Now one can, for example, separate these distributions,

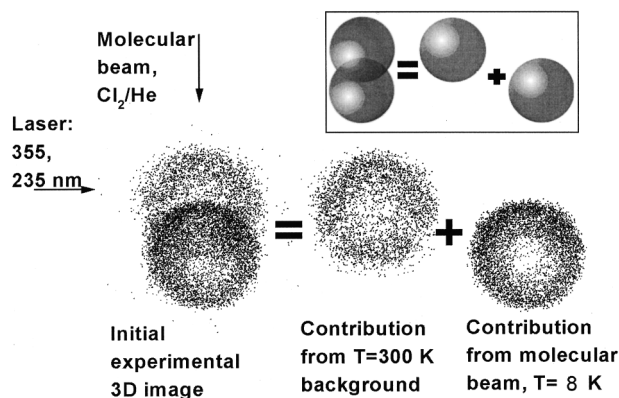


FIG. 9. The experimental 3D distribution of Cl atoms consists of two overlapping parts: one due to background Cl_2 at $T=300\text{ K}$, and another one due to cold Cl_2 in the molecular beam. They can easily be separated in three-dimensional space which is not possible with conventional 2D imaging. In the upper right corner this separation procedure is shown schematically: the experimental 3D spherical distributions are represented by half-transparent spheres.

as is schematically shown in Fig. 9, and study the speed distribution from the dissociation of cold molecules and warm molecules separately. Note that mathematically the separation of two 3D spheres with thin “walls” is a much more correct procedure than separations of the 2D projections of these spheres since the two spheres overlap only along a narrow ring in the 3D space, while the 2D projections of these spheres overlap strongly.

B. Speed distribution of Cl atoms

For illustrative purposes let us discuss the experiments presented in Figs. 9 and 10. The speed distributions of Cl atoms was fitted to the Gaussian distribution:

$$P(v) \propto e^{-(v-v_0)^2/2\sigma^2},$$

with $\Delta v = 2\sigma$ the full width of the speed distribution. The experimental values are $\Delta v' = 190\text{ m/s}$ and $\Delta v'' = 450\text{ m/s}$; hereafter one prime and two primes correspond to Cl_2/He molecular beam conditions ($T = 8 \pm 2\text{ K}$) and room temperature conditions ($T = 295\text{ K}$), respectively. The average speed of Cl atoms is equal to $v_0 = 1680\text{ m/s}$, it may be calculated

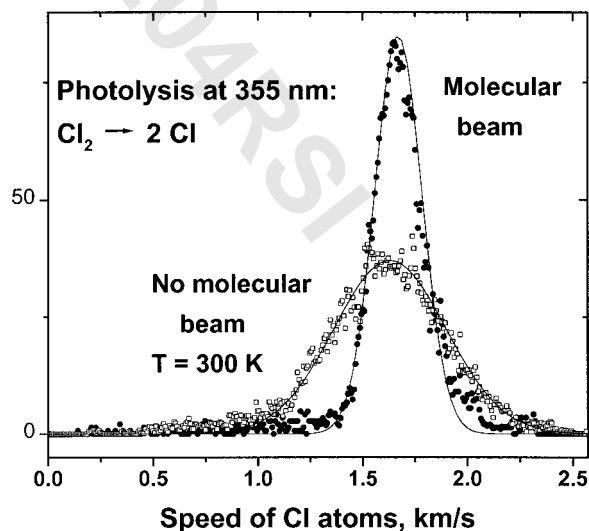


FIG. 10. Speed distribution of Cl atoms obtained from the 3D images in Fig. 9. Wide and narrow distributions correspond to the room temperature and Cl_2/He molecular beam conditions, respectively. The radius of the 3D distribution is 11.3 mm, the electric field is 30 V/cm, and the average time-of-flight is $7.4\ \mu\text{s}$.

TABLE II. Contributions to the width of the speed distribution of Cl atoms.

	Axis ^a	$\Delta v/\text{mm}^b$	$\Delta v/\text{m/s}$
Experimental data ^c	X,Y,Z	1.5 [3.0]	240 [450] ^d
	Z	1.1	160 ^d
Contributions from:			
T - R energy of Cl ₂ ^c	X,Y,Z	0.35 [2.8] ^e	53 [420]
- R energy of Cl ₂ ^c	X,Y,Z	0.30 [1.8] ^e	43 [270]
- T energy Cl ₂ ^c	Y	0.20 [2.2] ^e	30 [325]
Space resolution of DLD	X,Y	0.37	55 ^d
Duration of laser pulse (5 ns)	X,Y,Z	0.30	45 ^d
Length of laser spot	X	≥ 0.2	$\geq 30^d$
Ionization of Cl atom ^f	X,Y,Z	0.21 ^e	31

^aThe axis along which the broadening occurs.

^b $\Delta v/\text{mm}$ refers to size of image on the DLD.

^cThe data obtained at room temperature conditions ($T=295$ K) are shown in squared brackets.

^dCalculated from $\Delta v/\text{mm}$.

^eCalculated from $\Delta v/\text{m/s}$.

^fThe speed distribution is not Gaussian; we assume $\Delta v=2v_{\text{Cl}}$. Here $v_{\text{Cl}}=15.6$ m/s is the recoil speed of Cl⁺ ions due to the ionization process.

from $M_{\text{Cl}}v_0^2/2=[hv-D_0]/2$, where hv is the energy of the dissociating photon, M_{Cl} is the mass of Cl atom, and D_0 is the dissociation energy for the atomization of the chlorine molecule.

Now we shall discuss the most important factors contributing to Δv , which are listed in Table II.

C. Contribution from rotation and translational energy of Cl₂

Among the most important factors which contribute to Δv are the rotational energy and the dispersion of translational energy of the Cl₂ molecules. This contribution to Δv may be calculated as

$$2[M_{\text{Cl}}(\Delta v)^2/2]=E_R+E_T, \quad (6)$$

where $E_R=kT$ and E_T are the rotational and the translational energies of the Cl₂ molecule in the molecular beam fixed coordinate system where the average speed of the molecules is zero. In the molecular beam the translational temperature characterizes only the movement along the Y axis, while the speeds along the X and the Z axes are negligible; hence $E_{T'}=kT/2$ and $E_{T''}=(3/2)kT$. From Eq. (6) we obtain $\Delta v'=53$ m/s and $\Delta v''=420$ m/s. For “warm” molecules the agreement with experiment is good, for “cold” molecules the experimental width is more than three times larger than the calculated one. Thus apart from temperature there must be some other influence.

D. Contribution from the length of the laser spot

Let us estimate the length of the laser spot. The best condition for REMPI detection is usually achieved with a two-lens configuration. In this configuration the laser beam is slightly expanded by the first expanding lens and then it is focused by the second focusing lens. The length of the laser spot (“depth of focus”) may be estimated as

$$L_{\text{LS}}=Cd f/d_0, \quad (7)$$

where f is the focal length of the focusing lens, d_0 is the diameter of the laser beam on the focusing lens, d is the

minimum beam diameter, and C is a factor which is different in different models, but typically $1 \leq C \leq 2$. For example, the diffraction-determined length of the laser spot may be taken as doubled Rayleigh range which means $C=1$.³⁸

There are two contributions of different nature to the diameter of the laser spot. We estimate the diameter as

$$d=d_{\text{diff}}+d_a, \quad (8)$$

where the diameters d_{diff} and d_a are determined by diffraction and by aberration, respectively. d_a may be obtained from third order aberration theory as

$$d_a=\frac{n^2-(2n+1)K+(n+2)K^2/n}{32(n-1)^2} \frac{d_0^3}{f^2}, \quad (9)$$

where n is the refraction index, K is a shape factor of the lens $K=R_2/(R_2-R_1)$, and R_1 and R_2 are radii of curvature. For a properly oriented plano-convex focusing lens ($K=1$) of index $n=1.5$, the bracketed factor is 0.073. The diffraction-determined diameter d_{diff} may be estimated by the diameter of the first minimum of the Airy diffraction pattern in the focal plane as

$$d_{\text{diff}}=2.44(\lambda f/d_0), \quad (10)$$

where λ is the wavelength of radiation. The distance between the lenses is assumed to be large so the laser beam which comes to the focusing lens is treated as parallel.

Note that our experiments were done with the single-lens configuration shown in Fig. 1. In this configuration a narrow laser beam is focused to the center of the ionization chamber with one focusing lens. Using the values from our experiments of $f=20$ cm, $d_0=2.6$ mm, and $\lambda=235$ nm, we find from Eqs. (7)–(10) that $L_{\text{LS}}=3.2$ mm. This estimate explains our rather large value of $\Delta v'$ (see Table II). Here we have assumed that $C=1$; even this value leads to a slightly overestimated value for L_{LS} . Also, the widths of speed distributions along Y and Z axes were ≈ 2 times smaller than that along the X axis. This fact agrees with the conclusion that the main contribution to the width $\Delta v'$ in Fig. 10 comes from the length of the laser spot.

Let us estimate the minimal possible length of the laser spot. Our estimate is based on the assumption that the smallest length of the laser spot corresponds to the smallest laser beam diameter, which may be found from the condition $d_{\text{diff}} = d_a$. From this condition using Eqs. (7)–(10) and assuming $C=1$, one can find $d = 15 \mu\text{m}$, $d_0 = 16 \text{mm}$, and finally $L_{\text{LS}} = 200 \mu\text{m}$. Note that it is rather difficult to obtain this minimal value since it is very sensitive to d_0 .

E. Discussion

Other less important contributions come from the space resolution of the PSD, from the duration of the laser pulse, and from the electron recoil in the ionization of Cl atom, for which data are listed in Table II. We may summarize the results of these considerations as follows: a precise measurement of the speed distribution of photofragments requires a cold molecular beam, a two-lens configuration, and a large diameter of the distribution image (that is, large time-of-flight).

The cooling of the molecular beam is important to avoid the contribution of the rotation energy and dispersion of translational energy of the parent molecules. For example, under our experimental conditions the lowest temperatures may be achieved by using Ar as a buffer gas and by increasing the distance between the nozzle and the skimmer.

The two-lens configuration is important to decrease the length of the laser spot. The theoretic estimate shows that the length may be made very small ($\sim 200 \mu\text{m}$), less than the space resolution of the DLD or phosphorous screen, but this minimization requires additional efforts. From Table II one can see that for the properly installed two-lens configuration the length of the laser spot is one of the less important factors. Note that for the “velocity map imaging” technique which has recently been proposed by Eppink and Parker⁴ the size of laser spot is of no importance; but this technique has no time resolution. Also, in many cases the speed distribution of the photofragments is rather smooth, hence the advantage of the “velocity map imaging” technique over our 3D imaging in space resolution becomes unimportant.

The diameter of the distribution image must be large. The larger the diameter is, the larger is the time-of-flight and the smaller are contributions from the length of the laser spot, from the space resolution of the PSD, and from the duration of the laser pulse. Unfortunately, it is not always possible to increase the time-of-flight. For example, in a study of ³⁵Cl atoms it is often useful to get rid of the contribution from the ³⁷Cl isotope; the separation of the isotopes in time may be achieved only at rather short times-of-flight.

V. FUTURE APPLICATIONS TO REACTION DYNAMICS

The 3D photofragment imaging technique has proved to be a powerful tool to study the velocity (speed and angle) distributions of the products of photodissociation processes. The progress is directly comparable with real three-dimensional (stereo) pictures relative to two-dimensional photographs.

Further applications of the 3D imaging technique will go in several directions. Generally, most promising are applica-

tions to systems without inherent cylindrical symmetry or to systems where the cylindrical symmetry is broken due to technical imperfections of the experiment. First, it is the study of photodissociation dynamics of simple molecules. For example, the velocity dependence of the β anisotropy parameter contains valuable information about important features of dissociation dynamics like the competition of decay channels, simultaneous excitation of excited states, and regions of the potential energy surfaces where transitions to neighboring potential energy surfaces might or might not occur. Our technique allows one to directly obtain the complete information about the dependence of the β parameter on the particle velocity v in a single measurement. Work is currently in progress to measure the $\beta(v)$ dependence of Cl atoms produced in the photoinduced three-body decay of COCl_2 , SOCl_2 , CSCl_2 , and S_2Cl_2 .³⁹ A second application of the 3D imaging technique may be the study of the photofragment angular momentum alignment as a function of recoil angle (v – J correlation) in photodissociation processes. Here, observing nonequilibrium M_J substate distributions of photoproducts generated by linearly or circularly polarized light allows one to study subtle details of the dynamics of the dissociation process. A third application of our technique may be the investigation of the dynamics of chemical reactions. Detailed information on the reaction dynamics can be obtained by aligning the reactants in crossed molecular beams or by photodissociation of suitable precursors by polarized light.

ACKNOWLEDGMENTS

The authors appreciate the large support of Dr. U. Titt and Dr. M. Roth. A. I. Chichinin gratefully thanks the support of the Alexander von Humboldt Foundation and T. Einfeld acknowledges the support of the Fond der chemischen Industrie. Various parts of the work were funded by the Deutsche Forschungsgemeinschaft (DFG) and the German-Israeli Foundation (GIF).

- ¹D. W. Chandler and P. L. Houston, *J. Chem. Phys.* **87**, 1445 (1987).
- ²M. N. R. Ashfold, I. R. Lambert, D. H. Mordaunt, G. P. Moreley, and C. M. Western, *J. Phys. Chem.* **96**, 2938 (1992).
- ³B. J. Whitaker, in *Research in Chemical Kinetics, Vol 1*, edited by R. G. Compton and G. Hancock (Elsevier, New York, 1993).
- ⁴A. T. J. B. Eppink and D. H. Parker, *Rev. Sci. Instrum.* **68**, 3477 (1997).
- ⁵C. Maul and K.-H. Gericke, *Int. Rev. Phys. Chem.* **16**, 1 (1997).
- ⁶A. J. R. Heck and D. W. Chandler, *Annu. Rev. Phys. Chem.* **46**, 335 (1995).
- ⁷R. N. Zare, *J. Chem. Phys.* **61**, 491 (1974).
- ⁸V. Aquilanti, D. Ascenzi, M. de Castro Vitores, F. Pirani, and D. Cappelletti, *J. Chem. Phys.* **111**, 2620 (1999).
- ⁹V. Aquilanti, D. Ascenzi, D. Cappelletti, and F. Pirani, *Nature (London)* **371**, 399 (1994).
- ¹⁰V. Aquilanti, D. Ascenzi, D. Cappelletti, and F. Pirani, *J. Phys. Chem.* **99**, 13620 (1995).
- ¹¹V. Aquilanti, D. Ascenzi, D. Cappelletti, R. Fedeli, and F. Pirani, *J. Phys. Chem. A* **101**, 7648 (1997).
- ¹²S. Harich and A. M. Wodtke, *J. Chem. Phys.* **107**, 5983 (1997).
- ¹³E. B. Anthony, W. Schade, M. J. Bastian, V. M. Bierbaum, and S. R. Leone, *J. Chem. Phys.* **106**, 5413 (1997).
- ¹⁴F. Pirani, D. Cappelletti, M. Bartolomei, V. Aquilanti, M. Scotoni, M. Vescovi, D. Ascenzi, and D. Bassi, *Phys. Rev. Lett.* **86**, 5035 (2001).
- ¹⁵Y. Wang, H. P. Looock, J. Cao, and C. X. W. Qian, *J. Chem. Phys.* **102**, 808 (1995).

- ¹⁶A. S. Bracker, E. R. Wouters, A. G. Suits, Y. T. Lee, and O. S. Vasyutinskii, *Phys. Rev. Lett.* **80**, 1626 (1998).
- ¹⁷A. S. Bracker, E. R. Wouters, A. G. Suits, and O. S. Vasyutinskii, *J. Chem. Phys.* **110**, 6749 (1999).
- ¹⁸D. P. de Bruijn and J. Los, *Rev. Sci. Instrum.* **53**, 1020 (1982).
- ¹⁹J. C. Brenot and M. Durup-Ferguson, in *State-Selected and State-to-State Ion-Molecule Reaction Dynamics, Part I: Experiment*, edited by C. Y. Ng and M. Baer (Wiley, New York, 1992).
- ²⁰H. Helm and P. C. Cosby, *J. Chem. Phys.* **86**, 6813 (1987).
- ²¹R. E. Continetti, D. R. Cyr, D. L. Osborn, D. J. Leahy, and D. M. Neumark, *J. Chem. Phys.* **99**, 2616 (1993).
- ²²C. Maul and K.-H. Gericke, *J. Phys. Chem. A* **104**, 2531 (2000).
- ²³M. Roth, C. Maul, K.-H. Gericke, T. Senga, and M. Kawasaki, *Chem. Phys. Lett.* **305**, 319 (1999).
- ²⁴C. Maul, T. Haas, K.-H. Gericke, and F. J. Comes, *J. Chem. Phys.* **102**, 3238 (1995).
- ²⁵C. Maul, T. Haas, and K.-H. Gericke, *J. Phys. Chem.* **101**, 6619 (1997).
- ²⁶N. Arepalli, N. Presser, D. Robie, and R. Gordon, *Chem. Phys. Lett.* **118**, 88 (1985).
- ²⁷M. Mons and I. Dimicoli, *J. Chem. Phys.* **90**, 4037 (1989).
- ²⁸S. E. Sobottka and M. B. Williams, *IEEE Trans. Nucl. Sci.* **35**, 348 (1988).
- ²⁹I. Ali, R. Dörner, O. Jagutzki, S. Nüttgens, V. Mergel, L. Spielberger, K. Khayyat, T. Vogt, and H. Bräuning, *Nucl. Instrum. Methods Phys. Res. B* **149**, 490 (1999).
- ³⁰M. Lampton, O. Siegmund, and R. Raffanti, *Rev. Sci. Instrum.* **58**, 2298 (1987).
- ³¹Z. Amitay and D. Zajfman, *Rev. Sci. Instrum.* **68**, 1387 (1997).
- ³²P. L. Houston, B. R. Cosofret, A. Dixit, S. M. Dylewski, J. D. Geiser, J. A. Müller, R. J. Wilson, P. J. Pisano, M. S. Westley, K. T. Lorenz, and D. W. Chandler (private communication).
- ³³R. B. Bernstein, *Chemical Dynamics via Molecular Beam and Laser Techniques, The Hinshelwood Lectures, Oxford, 1980* (Clarendon Press, Oxford, 1982), p. 30.
- ³⁴D. R. Miller, in *Atomic and Molecular Beam Methods, vol 1*, edited by G. Scoles (Oxford University, New York, 1988), p. 14.
- ³⁵I. Kovacs, *Rotational Structure in the Spectra of Diatomic Molecules* (Adam Hilger, London, 1969), p. 130.
- ³⁶J. Park, Y. Lee, and G. W. Flynn, *Chem. Phys. Lett.* **186**, 441 (1991).
- ³⁷A. I. Chichinin, *Chem. Phys. Lett.* **209**, 459 (1993).
- ³⁸D. C. Moore, T. Vo-Dihn, N. H. Velthorst, and B. Schrader, *Laser-based Molecular Spectroscopy for Chemical Analysis-Laser Fundamentals* (Analytical chemistry division, Commission on spectrochemical and other optical procedures for analysis, IUPAC Recommendations 1994).
- ³⁹T. Einfeld, A. I. Chichinin, C. Maul, and K.-H. Gericke, *J. Chem. Phys.* (to be published).